

Received January 16, 2021, accepted January 29, 2021, date of publication February 8, 2021, date of current version February 17, 2021.

Digital Object Identifier 10.1109/ACCESS.2021.3057716

Analytical Modeling of Surface-Mounted and Consequent-Pole Linear Vernier Hybrid Machines

CHRISTOFF D. BOTHA¹, (Graduate Student Member, IEEE), MAARTEN J. KAMPER¹, (Senior Member, IEEE), RONG-JIE WANG¹, (Senior Member, IEEE), AND ABDOULKADRI CHAMA²

¹Department of Electrical and Electronic Engineering, Stellenbosch University, Stellenbosch 7600, South Africa

²Marine Research Institute, University of Cape Town, Rondebosch 7701, South Africa

Corresponding author: Christoff D. Botha (17058945@sun.ac.za)

This work was supported by the Centre for Renewable and Sustainable Energy Studies (CRSES) at Stellenbosch University, South Africa.

ABSTRACT This paper presents an analytical method for modeling the no-load air gap flux density of a surface-mounted and a consequent-pole linear Vernier hybrid machine (LVHM). The approach is based on simple magneto-motive force (MMF) and permeance functions to account for the doubly-slotted air gap of the LVHM. These models are used to determine the flux linkage, induced electromotive force (EMF) and average thrust force of each machine. The accuracy of the two analytical models is validated by comparison with 2D finite element method (FEM) solutions. Based on the analytical models, it is found that the working harmonics of both surface-mounted and consequent-pole LVHMs are essentially the same. However, the magnitudes of these working harmonics in the consequent-pole LVHM are invariably greater than those of surface-mounted LVHM. Further, using the analytical model, the contribution to the thrust force of the machine by each individual working harmonic can be shown clearly, and is used to explain why the consequent-pole LVHM has improved performance despite using only 50% of the permanent magnet (PM) material compared to the surface-mounted LVHM.

INDEX TERMS Air gap permeance, analytical method, consequent-pole, flux modulation, magneto-motive force, vernier machines.

NOMENCLATURE

B	flux density
\mathcal{F}	magnetomotive force
Λ	air gap permeance
\mathcal{R}	reluctance
μ_0	permeability of free space
μ_r	relative permeability of PMs
w_{PM}	width of PM
h_m	thickness of PM
SO	mover slot opening
l_{st}	stack length
l_m	mover length
g	air gap
Z_r	number of active translator teeth
Z_m	number of mover teeth
$\delta, \delta_m, \delta_r$	function describing additional air gap due to the slotting effect
a, b	fourier coefficients

h	harmonic component
N_s	number of series turns per phase

I. INTRODUCTION

The use of linear electrical machines in direct-drive applications has become increasingly attractive, as they eliminate the need for intermediate linear-to-rotary conversion systems. This is especially true for applications in which a slow linear motion is used to convert mechanical energy into electrical energy, such as wave energy generators and energy storage applications.

Although there are a number of electrical machine technologies, the variable reluctance permanent magnet (PM) machine technologies are particularly well-suited for these low-velocity and high-force direct-drive applications. These machines operate according to the flux modulation principle, where the PM field magneto-motive force (MMF) is modulated by a varying air gap permeance. A common problem for these machines, however, is the large leakage flux component, which causes a reduction in the main flux and an inherently low power factor [1], [2].

The associate editor coordinating the review of this manuscript and approving it for publication was Xiaodong Liang¹.

To improve magnet utilization and machine performance, the consequent pole (CP) technique, in which either the north or south pole magnets are replaced by soft ferromagnetic poles, can be used [1], [3], [4]. The CP technique has been studied in the literature for Vernier machines [1], [5]–[9] and flux-reversal machines (FRM) [2]–[4], [10]–[12]. While most of the research has focused on the working principle and optimal design solutions of CP machines, some research work has attempted to explain the potential advantages of the CP structure. In [4], a comparison of the pole leakage flux between a conventional and CP FRM based on a simplified magnetic circuit is used to explain the reduced leakage flux in, and thus improved performance of, the CP machine. More recently, the analytical model of the air gap flux density of a CP FRM was used to demonstrate how the asymmetric air gap field distribution of the CP machine leads to better torque production [2].

A. THE LINEAR VERNIER HYBRID MACHINE

The linear Vernier hybrid machine (LVHM) is a special type of variable reluctance machine, first introduced in [13] as a machine that possesses the high specific torque of a transverse-flux machine along with the simple construction of a flux-reversal machine. Further development of the technology for wave energy generator applications can be found in [1], [8], [14].

The surface-mounted (SM) and CP LVHMs considered in this paper are shown in Fig. 1. Both LVHMs consist of a mover and a translator. The mover carries a three-phase winding and PMs, while the translator is a passive and toothed structure. The only difference between the SM and CP LVHMs is in the PM arrangement, where all the south-pole magnets of the SM LVHM are replaced by ferromagnetic poles in the CP LVHM. Thus, the CP LVHM uses 50% less PMs than the SM LVHM.

Both machines operate on the principle of flux modulation, often referred to as the magnetic gearing principle, where the magnets create a multi-pole MMF in the air gap, which is then modulated by the varying permeance of the slotted translator. As multiple PMs link a single armature coil, the rate of change of flux is relatively high when compared with the mechanical movement speed, and the resulting induced EMF has an elevated frequency and magnitude.

A few analytical models have been proposed for SM Vernier hybrid machines (VHMs), although they are mostly for the rotary VHM. In [13], the shear stress equation of a rotary VHM was derived using the Lorenz force approach. In [15], an analytical model of the rotary VHM is presented based on a set of compact vector-matrix expressions, which was used to generate the co-energy map of the machine for analysing the VHM and developing a suitable machine control. A sub-domain model of the rotary VHM was developed in [16] to determine the no-load and on-load air gap flux densities and analyse the performance characteristics of the machine. However, there is little

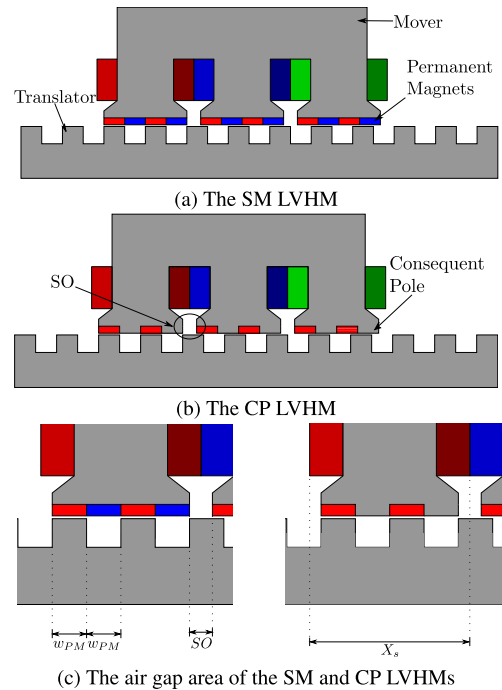


FIGURE 1. The linear Vernier hybrid machines, (a) SM LVHM and (b) CP LVHM, and (c) a closer image of the air gap area of the SM and CP LVHM, with some dimensions.

work on the analytical modeling of the CP LVHM in the literature.

The CP LVHM, described in [1], uses only half the amount of the PM material but shows better overall performance than the SM LVHM, with an improved thrust force and power factor and reduced cogging/ripple forces [1], [14]. Similar to [4], a magnetic equivalent circuit (MEC) representing the PM-to-consequent-pole flux pattern is used to explain the reduction in flux leakage and associated performance improvement in [1]. Generally, these over-simplified models are unsuitable for more in-depth analysis of the air gap field distribution and force-producing mechanisms of LVHMs.

In this paper, the analytical models of the air gap flux density for both SM and CP LVHMs are developed based on MMF-permeance theory. The emphasis is placed on making these analytical models more coherent, which allows a clear explanation of the force-production mechanisms and a direct performance comparison between the SM and CP LVHMs.

The remainder of the paper is organized as follows: In Section II, the development of two analytical models is described, and these are used to analyse the air gap field distribution and to identify the contributing field harmonics of the SM and CP LVHMs, respectively. In Section III, the analytical models are used to predict the flux linkage and induced EMF and the average electromagnetic thrust forces of both the SM and CP LVHMs, which are validated by comparing with the FEM results. Relevant conclusions are drawn in Section IV.

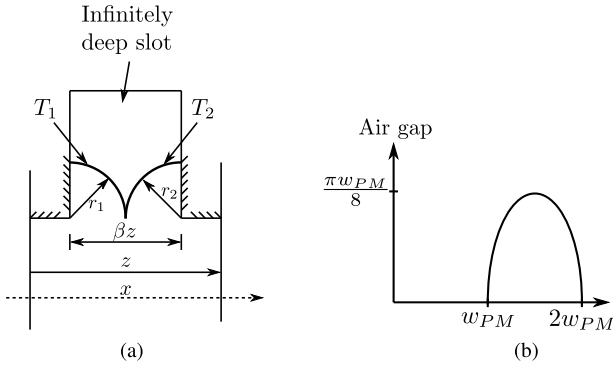


FIGURE 3. Illustrations of (a) the ideal slot and flux path used for calculating δ , and (b) the additional air gap due to translator slotting over a translator tooth pitch.

the slot opening, z being the pole/tooth pitch and T_1, T_2 being the ideal flux paths. For $\delta_m(x)$, $\beta z = SO$ and $z = X_s$, and for $\delta_r(x, t)$, $\beta z = w_{PM}$ and $z = 2w_{PM}$, as illustrated in Fig. 1 (c). Assuming quarter-circle flux lines, the arc lengths can be given as: $T_1 = \frac{\pi}{2}x$ and $T_2 = \frac{\pi}{2}(\beta z - x)$.

The general slotting function is equal to the equivalent length of the idealised flux lines, i.e. $T_1 || T_2$ in Fig. 3, and is given as

$$\delta(x) = \frac{\pi}{2} \left(\frac{\beta z x - x^2}{\beta z} \right). \quad (7)$$

Fig. 3 (b) is the graphic representation of (7) as it applies to a translator tooth pitch. From Fig. 1 (c) and the function definition of $\mathcal{F}_{SM}(x)$ (Fig. 2), it can be noted that the mover slotting only occurs where $\mathcal{F}_{SM}(x) = 0$, and thus $\Lambda_{SM}(x, t)$ can be simplified by ignoring $\delta_m(x)$.

The Fourier series equivalent of $\Lambda_{SM}(x, t)$ can then be expressed as

$$\Lambda_{SM}(x, t) = \frac{a_0^s}{2} + \sum_{j=1}^{\infty} a_j^s \cos \left(\omega_j \left(x + \frac{k_1}{2} + vt \right) \right), \quad (8)$$

with $\omega_j = jZ_r \frac{2\pi}{l_m}$, Z_r being the number of active translator teeth and v being the mover velocity. Here, a_0^s is

$$a_0^s = \frac{1}{g'} + \frac{2}{d_1} \left(\ln \left(\frac{d_2}{d_3} \right) - \ln \left(\frac{(d_3)^2}{8k_2\pi g'} \right) \right), \quad (9)$$

with $d_1 = \sqrt{(\pi k_2)^2 + 8k_2\pi g'}$, $d_2 = d_1 + \pi k_2$ and $d_3 = d_1 - \pi k_2$; a_j^s is given by

$$a_j^s = \frac{-2}{g'j\pi} \sin \left(\frac{j\pi}{2} \right) + \int_{-\frac{k_2}{2}}^{\frac{k_2}{2}} \frac{\cos(\omega_j x)}{g' + \alpha \left(x - \frac{k_2}{2} \right) \left(x + \frac{k_2}{2} \right)} dx, \quad (10)$$

with $\alpha = -\frac{\pi}{2k_2}$.

3) AIR GAP FLUX DENSITY

Substituting (4) and (8) into (2), and keeping in mind that only the fundamental harmonic of Λ_{SM} contributes to the induced

EMF and the force production, i.e. $j = 1$ in (8), the SM LVHM's no-load air gap flux density can be written as

$$\begin{aligned} B_{SM}(x, t) &= \mu_0 \mathcal{F}_{SM}(x) \Lambda_{SM}(x, vt) \\ &= \mu_0 \sum_{i=1}^{\infty} \left[\frac{a_0^s b_i^s}{2} \sin(\chi_i^1(x)) \right. \\ &\quad \left. + \frac{a_1^s b_i^s}{2} \sin(\chi_i^1(x) - \vartheta_1(x, t)) \right. \\ &\quad \left. + \frac{a_1^s b_i^s}{2} \sin(\chi_i^1(x) + \vartheta_1(x, t)) \right], \quad (11) \end{aligned}$$

where $\chi_i^1(x) = \omega_i x$ and $\vartheta_1(x, t) = \omega_1 \left(x + \frac{k_1}{2} + vt \right)$. The specific harmonic components of the SM LVHM can be found by expanding each sine term. For example, $\chi_i^1(x) - \vartheta_1(x, t)$ can be expressed as below.

$$\begin{aligned} \chi_i^1(x) - \vartheta_1(x, t) &= \omega_i x - \omega_1 \left(x + \frac{k_1}{2} + vt \right) \\ &= (iZ_m - Z_r) \frac{2\pi}{l_m} x \\ &\quad - Z_r \frac{2\pi}{l_m} \left(\frac{k_1}{2} + vt \right) \quad (12) \end{aligned}$$

Following a similar process, three main harmonic components can be identified from (11), viz.

$$h_1^s = |iZ_m| \quad (13)$$

$$h_2^s = |iZ_m - Z_r| \quad (14)$$

$$h_3^s = |iZ_m + Z_r| \quad (15)$$

A comparison of the FEM and analytically calculated air gap flux densities is shown in Fig. 4, with the analytically derived flux density agreeing well with the result obtained from 2D FEM.

B. CONSEQUENT-POLE LINEAR VERNIER HYBRID MACHINE

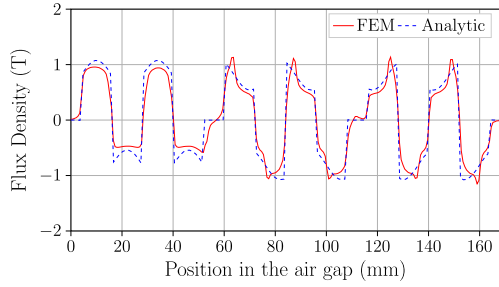
Similar to the SM LVHM, the no-load air gap flux density of the CP LVHM can be given by

$$B_{CP}(x, t) = \mu_0 \mathcal{F}_{CP}(x) \Lambda_{CP}(x, t). \quad (16)$$

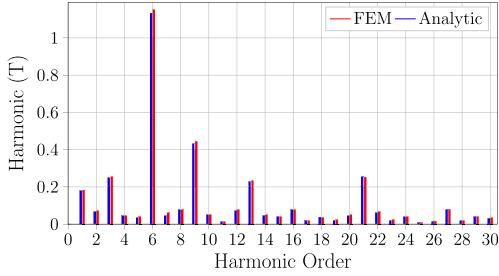
1) MAGNETO-MOTIVE FORCE

The MMF distribution created by the consequent-pole structure can be defined as

$$\mathcal{F}_{CP}(x) = \begin{cases} 0; & 0 \leq x < \frac{SO}{2} \\ \mathcal{F}'_m; & \frac{SO}{2} \leq x < \frac{SO}{2} + w_{PM} \\ -\mathcal{F}'_i; & \frac{SO}{2} + w_{PM} \leq x < \frac{SO}{2} + 2w_{PM} \\ \mathcal{F}'_m; & \frac{SO}{2} + 2w_{PM} \leq x < \frac{SO}{2} + 3w_{PM} \\ -\mathcal{F}'_i; & \frac{SO}{2} + 3w_{PM} \leq x < \frac{SO}{2} + 4w_{PM} \\ 0; & \frac{SO}{2} + 4w_{PM} \leq x < X_s \end{cases} \quad (17)$$



(a) Comparing the FEM and analytically derived $B_{SM}(x, t)$ at $t = 0$



(b) The harmonic spectra of $B_{SM}(x, t)$

FIGURE 4. Comparison of the FEM and analytical prediction of (a) the no-load air gap flux density, and (b) the harmonic spectra of the no-load air gap flux density of the SM LVHM.

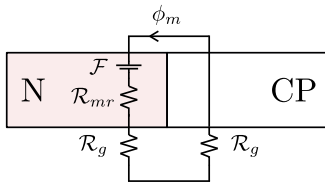


FIGURE 5. A simple magnetic circuit of the consequent-pole structure with a slotless translator and air gap g .

In the above equation, \mathcal{F}'_m and \mathcal{F}_t are the adjusted magnitudes of the air gap MMF underneath the PM and the consequent-pole, respectively. The values can be determined using the simple magnetic circuit in Fig. 5, where $\mathcal{F} = \frac{B_r l_m}{\mu_r \mu_0}$, \mathcal{R}_{mr} is the magnet reluctance and \mathcal{R}_g is the air gap reluctance.

From this circuit, the flux, ϕ_m , can be calculated as

$$\phi_m = \frac{\mathcal{F}}{\mathcal{R}_{mr} + 2\mathcal{R}_g}, \quad (18)$$

with

$$\mathcal{R}_{mr} = \frac{h_m}{\mu_0 \mu_r w_{PM} l_{st}}, \quad (19)$$

$$\mathcal{R}_g = \frac{g}{\mu_0 w_{PM} l_{st}}, \quad (20)$$

with l_{st} being the machine stack length and g the air gap. Using equations (18) to (20), a simple estimate for \mathcal{F}'_m and \mathcal{F}_t can be given as

$$\mathcal{F}'_m = \phi_m (\mathcal{R}_{mr} + \mathcal{R}_g), \quad (21)$$

$$\mathcal{F}_t = \phi_m \mathcal{R}_g. \quad (22)$$

The air gap MMF of the CP LVHM, shown in Fig. 6, is thus asymmetrical.

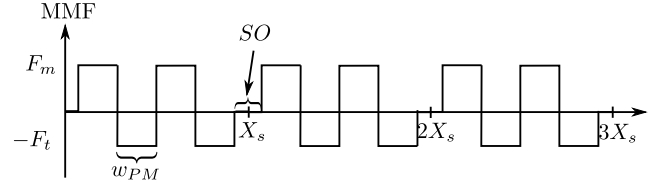


FIGURE 6. The MMF waveform of the CP LVHM.

2) AIR GAP PERMEANCE

The CP LVHM air gap permeance function, $\Lambda_{CP}(x, t)$, is defined as

$$\Lambda_{CP}(x, t) = \frac{1}{\delta_{CP}(x) + \delta_r(x, t)}, \quad (23)$$

where $\delta_{CP}(x)$ replaces g' from $\Lambda_{SM}(x, t)$ in (6) and is the slotting effect due to the consequent-poles, defined as in (24).

$$\delta_{CP}(x) = \begin{cases} g; & 0 \leq x < \frac{SO}{2} \\ g'; & \frac{SO}{2} \leq x < \frac{SO}{2} + w_{PM} \\ g; & \frac{SO}{2} + w_{PM} \leq x < \frac{SO}{2} + 2w_{PM} \\ g'; & \frac{SO}{2} + 2w_{PM} \leq x < \frac{SO}{2} + 3w_{PM} \\ g; & \frac{SO}{2} + 3w_{PM} \leq x < \frac{SO}{2} + 4w_{PM} \\ g; & \frac{SO}{2} + 4w_{PM} \leq x < X_s \end{cases} \quad (24)$$

3) SIMPLIFIED APPROACH USING SUPERPOSITION

It is clear from equations (17) and (23) that the functions describing the air gap flux density of the CP LVHM are more complex due to the soft ferromagnetic pole. To alleviate the complexity, the analytical model is divided into two separate solutions, as explained below.

Using the principle of superposition, the MMF function can be expressed as:

$$\mathcal{F}_{CP}(x) = \mathcal{F}_{CP}^1(x) + \mathcal{F}_{CP}^2(x), \quad (25)$$

with \mathcal{F}_{CP}^1 and \mathcal{F}_{CP}^2 representing the MMF underneath the magnet and the consequent-pole, respectively. Their function definitions are given below.

$$\mathcal{F}_{CP}^1(x) = \begin{cases} 0; & 0 \leq x < \frac{SO}{2} \\ \mathcal{F}'_m; & \frac{SO}{2} \leq x < \frac{SO}{2} + w_{PM} \\ 0; & \frac{SO}{2} + w_{PM} \leq x < \frac{SO}{2} + 2w_{PM} \\ \mathcal{F}'_m; & \frac{SO}{2} + 2w_{PM} \leq x < \frac{SO}{2} + 3w_{PM} \\ 0; & \frac{SO}{2} + 3w_{PM} \leq x < \frac{SO}{2} + 4w_{PM} \\ 0; & \frac{SO}{2} + 4w_{PM} \leq x < X_s \end{cases} \quad (26)$$

$$\mathcal{F}_{CP}^2(x) = \begin{cases} 0; & 0 \leq x < \frac{SO}{2} \\ 0; & \frac{SO}{2} \leq x < \frac{SO}{2} + w_{PM} \\ -\mathcal{F}_t; & \frac{SO}{2} + w_{PM} \leq x < \frac{SO}{2} + 2w_{PM} \\ 0; & \frac{SO}{2} + 2w_{PM} \leq x < \frac{SO}{2} + 3w_{PM} \\ -\mathcal{F}_t; & \frac{SO}{2} + 3w_{PM} \leq x < \frac{SO}{2} + 4w_{PM} \\ 0; & \frac{SO}{2} + 4w_{PM} \leq x < X_s \end{cases} \quad (27)$$

The Fourier series equivalents are

$$\mathcal{F}_{CP}^1(x) = \frac{a_0^{c1}}{2} + \sum_{i=1}^{\infty} a_i^{c1} \cos\left(\omega_i \left(x + \frac{3k_1}{8}\right)\right), \quad (28)$$

$$\mathcal{F}_{CP}^2(x) = \frac{a_0^{c2}}{2} + \sum_{i=1}^{\infty} a_i^{c2} \cos\left(\omega_i \left(x - \frac{3k_1}{8}\right)\right), \quad (29)$$

with the superscript *c* indicating that it is a variable related to the CP LVHM. The relevant coefficients are given as:

$$a_0^{c1} = \frac{6}{7} \mathcal{F}'_m, \quad (30)$$

$$a_i^{c1} = \frac{2\mathcal{F}'_m}{i\pi} \left(\sin(i\pi \frac{11}{14}) - \sin(i\pi \frac{5}{14}) \right), \quad (31)$$

$$a_0^{c2} = \frac{6}{7} \mathcal{F}'_t, \quad (32)$$

$$a_i^{c2} = \frac{2\mathcal{F}'_t}{i\pi} \left(\sin(i\pi \frac{11}{14}) - \sin(i\pi \frac{5}{14}) \right). \quad (33)$$

From (24) and the function definitions of F_{CP}^1 and F_{CP}^2 , it is evident that $\delta_{CP}(x) = g'$ where $\mathcal{F}_{CP}^1 \neq 0$, and that $\delta_{CP}(x) = g$ where $\mathcal{F}_{CP}^2 \neq 0$.

Similarly, Λ_{CP} can also be split into $\Lambda_{CP}^1(x, t)$ and $\Lambda_{CP}^2(x, t)$, as

$$\Lambda_{CP}^1(x, t) = \frac{1}{g' + \delta_r(x, t)}, \quad (34)$$

$$\Lambda_{CP}^2(x, t) = \frac{1}{g + \delta_r(x, t)}. \quad (35)$$

The Fourier series equivalents are given by

$$\Lambda_{CP}^1(x, t) = \Lambda_{SM}(x, t), \quad (36)$$

$$\Lambda_{CP}^2(x, t) = \frac{a_0^{c3}}{2} + \sum_{j=1}^{\infty} a_j^c \cos\left[\omega_j \left(x + \frac{k_1}{2} + vt\right)\right]. \quad (37)$$

The coefficients a_0^{c3} and a_j^c are the same as the coefficients for Λ_{SM} , only with g' being replaced by g .

4) AIR GAP FLUX DENSITY

$B_{CP}(x, t)$ can thus be written as

$$B_{CP}(x, t) = \mu_0 \left[\mathcal{F}_{CP}^1(x) \Lambda_{CP}^1(x, t) + \mathcal{F}_{CP}^2(x) \Lambda_{CP}^2(x, t) \right], \quad (38)$$

which can then be expanded as

$$\begin{aligned} B_{CP}(x, t) &= \mu_0 \left[\mathcal{F}_{CP}^1(x) \Lambda_{CP}^1(x, t) + \mathcal{F}_{CP}^2(x) \Lambda_{CP}^2(x, t) \right] \\ &= \mu_0 \left[\frac{a_0^{c1} a_0^s}{4} + \frac{a_0^{c2} a_0^{c3}}{4} \right. \\ &\quad + \left(\frac{a_0^{c1} a_1^s}{2} + \frac{a_0^{c2} a_1^c}{2} \right) \cos(\vartheta_1(x, t)) \\ &\quad + \sum_{i=1}^{\infty} \frac{a_i^{c1} a_0^s}{2} \cos(\chi_i^2(x)) + \frac{a_i^{c2} a_0^{c3}}{2} \cos(\chi_i^3(x)) \\ &\quad + \sum_{i=1}^{\infty} \frac{a_i^{c1} a_1^s}{2} \cos(\chi_i^2(x) - \vartheta_1(x, t)) \\ &\quad + \frac{a_i^{c2} a_1^s}{2} \cos(\chi_i^3(x) - \vartheta_1(x, t)) \\ &\quad + \sum_{i=1}^{\infty} \frac{a_i^{c1} a_1^c}{2} \cos(\chi_i^2(x) + \vartheta_1(x, t)) \\ &\quad \left. + \frac{a_i^{c2} a_1^c}{2} \cos(\chi_i^3(x) + \vartheta_1(x, t)) \right], \quad (39) \end{aligned}$$

where $\chi_i^2(x) = \omega_i(x + \frac{3k_1}{8})$ and $\chi_i^3(x) = \omega_i(x - \frac{3k_1}{8})$.

With this formulation of the air gap flux density, and following the same process as detailed for the SM LVHM, it can be found that the CP LVHM has the following field harmonics in the air gap:

$$h_1^c = |iZ_m| \quad (40)$$

$$h_2^c = |Z_r| \quad (41)$$

$$h_3^c = |iZ_m - Z_r| \quad (42)$$

$$h_4^c = |iZ_m + Z_r| \quad (43)$$

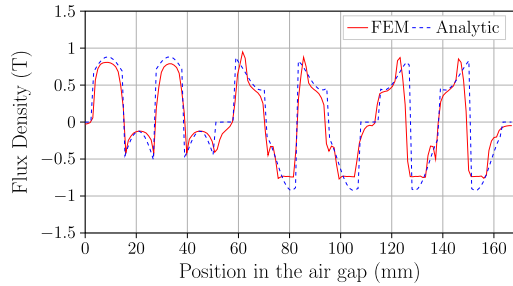
A comparison of the FEM and analytical air gap flux densities and harmonic spectra are shown in Fig. 7, illustrating good agreement between the two.

III. COMPARISON OF THE SM AND CP LVHM

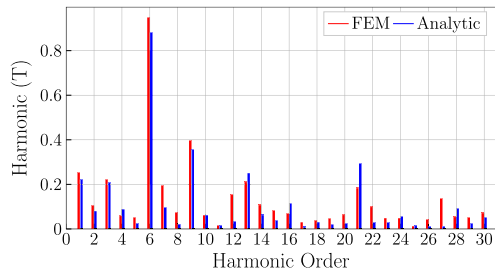
Using the analytical models derived in the previous section, the flux linkage, induced EMF and thrust force can be determined for both LVHMs. The phase flux linkage can be determined directly from the air gap flux density by

$$\lambda_{ph}(t) = (N_s k_d k_p) g l_{st} \int_{\mathcal{S}} B(x, t) dx, \quad (44)$$

where the set \mathcal{S} indicates integration over a mover pole pitch, N_s is the number of turns in series per phase, k_d is the distribution factor and k_p the coil-span factor. The no-load



(a) Comparison of the FEM and analytically derived CP LVHM air gap flux density at $t = 0$



(b) The harmonic spectra of the CP LVHM air gap flux density

FIGURE 7. Comparison of the FEM and analytical prediction of the (a) air gap flux density and (b) harmonic spectra of the CP LVHM.

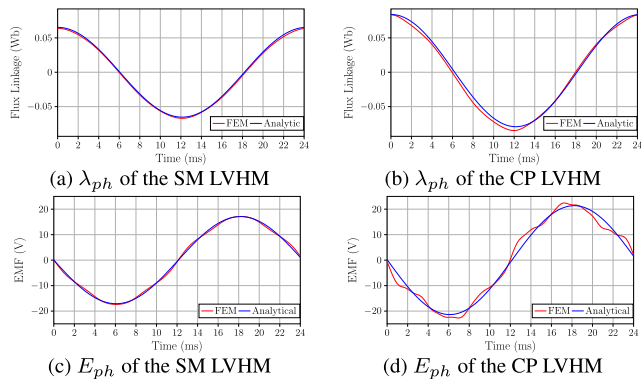


FIGURE 8. Comparison of the FEM and analytically predicted phase flux linkage for the (a) SM and (b) CP LVHM, and the induced EMF for the (c) SM and (d) CP LVHM.

induced EMF is given as

$$e_{ph}(t) = -\frac{d}{dt} \lambda_{ph}(t). \quad (45)$$

The comparison between the FEM-derived and analytical prediction for the flux linkage and no-load EMF of both machines is shown in Fig. 8. The finite element models showing the flux distribution of both the SM and CP LVHMs are given in Fig. 9. A prediction of the thrust force can then be made using the analytical model as

$$f_{an}(t) = \sum_{i=A,B,C} e_{iph}(t) i_i(t), \quad (46)$$

with $i_{iph}(t)$ being the phase currents. The average thrust force from the FEM results, F_{FEM} , and the analytically derived average thrust force, F_{an} , are compared in Table 2.

It is evident from Fig. 8 and Table 2 that the results of the analytical models correlate well with those of FEM.

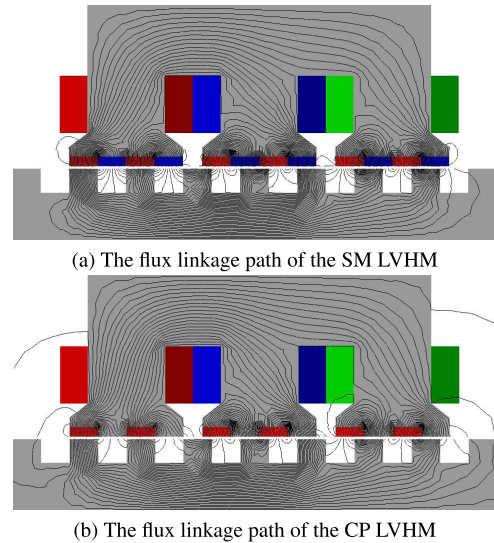


FIGURE 9. The finite element models showing flux distribution of the (a) SM LVHM and (b) CP LVHM.

TABLE 2. Force comparison.

	SM LVHM	CP LVHM
F_{FEM} (N)	171.55	216.3
F_{an} (N)	173.5	214.3

The model of the SM LVHM closely matches the FEM in flux linkage, induced EMF and average thrust force. The CP LVHM model does not have the same accuracy as the SM LVHM, especially when comparing the induced EMF with FEM. This is likely due to the presence of other permeance harmonics that are not taken into account in the analytical model. However, these harmonics make practically no contribution to the force production, as the average thrust force obtained from the analytical model and from 2D FEM are very similar.

The CP LVHM clearly has a higher flux linkage and induced EMF magnitude, leading to a 25% increase in the average thrust force. Using (11), (39) and (44) to (46), the effect of each harmonic on the force production of the two machines can be determined. Table 3 provides this comparison, with h_1^s , h_1^c and h_2^c omitted, as they are stationary harmonics and do not contribute to the force production [2].

From these results it is clear that the 1st, 2nd and 4th harmonics contribute to the force production, with the 1st harmonic being the most important. It is interesting to note that, for both LVHMs, the $iZ_m - Z_r$ component, i.e. the lower-order harmonics, is the main contributor to their force production, with the $iZ_m + Z_r$ component, i.e. the higher-order harmonics, constituting a ripple flux component. Table 4 summarizes the percentage contribution of the main harmonics in the SM and CP LVHMs to the average thrust force.

From Table 3 it is evident that both LVHMs have exactly the same order field harmonics that contribute to the force production, and Table 4 shows that the different harmonics

TABLE 3. The order and magnitude of the harmonic spectra for the SM LVHM and CP LVHM.

		SM LVHM		CP LVHM	
		h_2^s	h_3^s	h_3^c	h_4^c
i = 1	Order	4	10	4	10
	Magnitude (T)	0.048	0.052	0.089	0.0623
	Force (N)	6.66	-2.2	9.11	-2.72
i = 2	Order	1	13	1	13
	Magnitude (T)	0.18	0.23	0.22	0.25
	Force (N)	139.69	-7.32	176.6	-10.66
i = 3	Order	2	16	2	16
	Magnitude (T)	0.072	0.079	0.081	0.114
	Force (N)	28.5	1.98	35.37	3.47
i = 4	Order	5	19	5	19
	Magnitude (T)	0.04	0.020	0.0236	0.021
	Force (N)	2	0.24	2.67	0.61
i = 5	Order	8	22	8	22
	Magnitude (T)	0.078	0.069	0.022	0.028
	Force (N)	-0.3775	-0.05	-0.29	0.03

TABLE 4. The percentage contribution of the main harmonics in the SM LVHM and CP LVHM to the average thrust force.

		SM LVHM			CP LVHM		
		Total	h_2^s	h_3^s	Total	h_3^c	h_4^c
i = 1	Order	4	10		4	10	
	%	2.57	3.89	-1.28	2.98	4.25	-1.27
i = 2	Order	1	13		1	13	
	%	77.25	81.52	-4.27	77.4	82.41	-4.97
i = 3	Order	2	16		2	16	
	%	17.79	16.63	1.16	18.12	16.5	1.62

have a similar percentage contribution to the force production. The improved performance of the CP LVHM can be attributed to the higher magnitudes of the three working harmonics. This can be explained in part by studying (11) and (39), specifically the lower-order harmonics of the SM and CP LVHMs.

When comparing the lower order harmonics, the most obvious difference comes from the terms determining the magnitude of these components. For the SM LVHM, the term is $(b_i^s) \frac{\alpha_i^s}{2}$, and for the CP LVHM it is $(a_i^{c1} + a_i^{c2}) \frac{\alpha_i^c}{2}$. The air gap flux density waveforms of both LVHMs due to the main working harmonic components are compared in Fig. 10, where the CP LVHM exhibits a larger flux density despite having less overall air gap flux density, as seen when comparing Fig. 4 (a) and Fig. 7 (a).

As the lower-order harmonics of both machines are a result of the interaction between the respective air gap MMF waveforms and the same permeance function, the main difference comes from the different MMF waveforms of the SM and CP LVHMs. While \mathcal{F}'_m is about 17 % smaller than \mathcal{F}_m , the difference between F_t and \mathcal{F}_m is much greater, with F_t being 83 % smaller than \mathcal{F}_m . The CP LVHM demonstrates an increased average thrust force despite this decrease in air gap MMF, which is somewhat counter-intuitive. This indicates that the magnet pole being replaced with the consequent-pole, in this case the south pole magnet, does not contribute

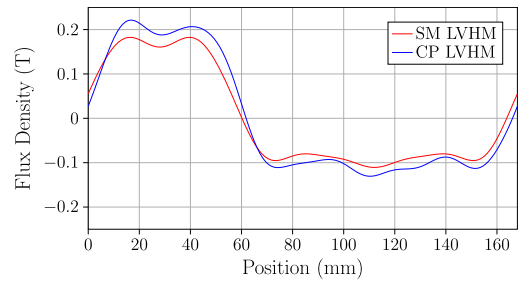


FIGURE 10. The air gap flux density at $t = 0$ due to the main working harmonics.

meaningfully towards the force generation, and likely only produces a leakage component, degrading the performance of the SM LVHM. This reduction in leakage flux is also evident when comparing the flux between the two PMs in the SM LVHM and between the PM and CP in the CP LVHM, in Fig. 9 (a) and (b), respectively.

Another interesting observation is that the percentage force contribution of higher-order harmonics, i.e. h_3^s and h_4^c , is similar between the SM and CP LVHMs. Since the higher-order field harmonics are mainly the source of pulsating flux and force, this indicates that the cogging and ripple forces of the CP LVHM would be greater than those of the SM LVHM. As discussed in the literature [7], [9], [18], [19], some techniques such as tapering the consequent-poles and translator teeth, are normally applied to reduce the flux leakage, mitigate the cogging/ripple forces, and provide a more sinusoidal induced EMF for CP LVHMs.

IV. CONCLUSION

In this paper, the analytical models for the no-load air gap flux density of the SM and CP LVHMs were derived based on MMF-permeance theory. The analytical models were used to determine the phase flux linkage, induced EMF and average thrust force of the machines.

Detailed comparisons with 2D FEM show that the developed analytical models accurately predict the no-load air gap field distributions of both machines. Their validity is further proved by comparing the determined phase flux linkages, induced EMFs and thrust forces with 2D FEM simulations.

By using the principle of superposition for the air gap MMF, the analytical modeling of the CP LVHM is not only simplified, but also forms a coherent set of air gap flux density equations that are easily comparable with the SM LVHM. A clear advantage of the developed analytical models therefore is that it enables a direct comparison of the individual harmonics and their contribution to the average thrust force.

In comparison with the SM LVHMs, the flux density equations clearly show that the consequent-pole technique does not introduce new working harmonics in the CP LVHMs, but only increases the magnitudes of these working harmonics. The improvement of the working harmonics in the CP LVHM leads to an increase of approximately 25 % in the magnitude of the flux linkage, induced EMF and thrust force when compared with the SM LVHM. Using these working harmonics,

this paper provides a clearer explanation of and greater insight into the performance improvement of the CP LVHMs.

REFERENCES

- [1] A. A. Almoraya, N. J. Baker, K. J. Smith, and M. A. H. Raihan, "Development of a double-sided consequent pole linear Vernier hybrid permanent-magnet machine for wave energy converters," in *Proc. IEEE Int. Electric Mach. Drives Conf. (IEMDC)*, May 2017, pp. 1–7.
- [2] H. Yang, Z. Q. Zhu, H. Lin, H. Li, and S. Lyu, "Analysis of consequent-pole flux reversal permanent magnet machine with biased flux modulation theory," *IEEE Trans. Ind. Electron.*, vol. 67, no. 3, pp. 2107–2121, Mar. 2020.
- [3] S.-U. Chung, H.-J. Lee, and S.-M. Hwang, "A novel design of linear synchronous motor using FRM topology," *IEEE Trans. Magn.*, vol. 44, no. 6, pp. 1514–1517, Jun. 2008.
- [4] Y. Gao, R. Qu, D. Li, J. Li, and G. Zhou, "Consequent-pole flux-reversal permanent-magnet machine for electric vehicle propulsion," *IEEE Trans. Appl. Supercond.*, vol. 26, no. 4, Jun. 2016, Art. no. 5200105.
- [5] X. Liu, C. Zou, Y. Du, and F. Xiao, "A linear consequent pole stator permanent magnet Vernier machine," in *Proc. 17th Int. Conf. Electr. Mach. Syst. (ICEMS)*, Oct. 2014, pp. 1753–1756.
- [6] C. Shi, R. Qu, D. Li, Y. Gao, and R. Li, "Comparative study on a novel consequent-pole modular linear Vernier machine with PMs on both mover and stator iron cores," in *Proc. IEEE Energy Convers. Congr. Expo. (ECCE)*, Sep. 2019, pp. 712–716.
- [7] Y. Zhou, R. Qu, Y. Gao, C. Shi, and C. Wang, "Modeling and analyzing a novel dual-flux-modulation consequent-pole linear permanent-magnet machine," *IEEE Trans. Magn.*, vol. 55, no. 7, Jul. 2019, Art. no. 8203906.
- [8] A. A. Almoraya, N. J. Baker, K. J. Smith, and M. A. H. Raihan, "Design and analysis of a flux-concentrated linear Vernier hybrid machine with consequent poles," *IEEE Trans. Ind. Appl.*, vol. 55, no. 5, pp. 4595–4604, Sep. 2019.
- [9] C. D. Botha, M. J. Kamper, R.-J. Wang, and A. J. Sorgdrager, "Force ripple and cogging force minimisation criteria of single-sided consequent-pole linear Vernier hybrid machines," in *Proc. Int. Conf. Electr. Mach. (ICEM)*, Aug. 2020, pp. 469–475.
- [10] H. Y. Li and Z. Q. Zhu, "Analysis of flux-reversal permanent-magnet machines with different consequent-pole PM topologies," *IEEE Trans. Magn.*, vol. 54, no. 11, pp. 1–5, Nov. 2018.
- [11] H. Qu, Z. Q. Zhu, and H. Li, "Analysis of novel consequent pole flux reversal permanent magnet machines," *IEEE Trans. Ind. Appl.*, vol. 57, no. 1, pp. 382–396, Jan. 2021.
- [12] H. Li and Z. Zhu, "Investigation of stator slot/rotor pole combination of flux reversal permanent magnet machine with consequent-pole PM structure," *J. Eng.*, vol. 2019, no. 17, pp. 4267–4272, Jun. 2019.
- [13] E. Spooner and L. Haydock, "Vernier hybrid machines," *IEE Proc.-Electr. Power Appl.*, vol. 150, no. 6, pp. 655–662, Nov. 2003.
- [14] N. J. Baker, M. A. H. Raihan, A. A. Almoraya, J. W. Burchell, and M. A. Mueller, "Evaluating alternative linear Vernier hybrid machine topologies for integration into wave energy converters," *IEEE Trans. Energy Convers.*, vol. 33, no. 4, pp. 2007–2017, Dec. 2018.
- [15] L. Papini, C. Gerada, and P. Bolognesi, "Comparison of analytical and FE modeling of Vernier hybrid machine," in *Proc. 10th Int. Conf. Electr. Mach.*, Sep. 2012, pp. 582–588.
- [16] Y. Yang, G. Liu, X. Yang, and X. Wang, "Analytical electromagnetic performance calculation of Vernier hybrid permanent magnet machine," *IEEE Trans. Magn.*, vol. 54, no. 6, Jun. 2018, Art. no. 8202612.
- [17] B. Gaussens, E. Hoang, O. de la Barriere, J. Saint-Michel, M. Lecrivain, and M. Gabssi, "Analytical approach for air-gap modeling of field-excited flux-switching machine: No-load operation," *IEEE Trans. Magn.*, vol. 48, no. 9, pp. 2505–2517, Sep. 2012.
- [18] X. Xu, Z. Sun, B. Du, and L. Ai, "Pole optimization and thrust ripple suppression of new Halbach consequent-pole PMLSM for ropeless elevator propulsion," *IEEE Access*, vol. 8, pp. 62042–62052, 2020.
- [19] J. Li, K. Wang, and F. Li, "Reduction of torque ripple in consequent-pole permanent magnet machines using staggered rotor," *IEEE Trans. Energy Convers.*, vol. 34, no. 2, pp. 643–651, Jun. 2019.



CHRISTOFF D. BOTHA (Graduate Student Member, IEEE) received the B.Eng. and M.Eng. degrees in electrical and electronic engineering from Stellenbosch University, South Africa, in 2015 and 2018, respectively, where he is currently pursuing the Ph.D. degree with the Department of Electrical and Electronic Engineering. His current research interests include linear electric machines and energy storage for use in renewable energy grid integration.



MAARTEN J. KAMPER (Senior Member, IEEE) received the M.Sc. (Eng.) and Ph.D. (Eng.) degrees from Stellenbosch University, South Africa, in 1987 and 1996, respectively. In 1989, he joined as an Academic Staff with the Department of Electrical and Electronic Engineering, Stellenbosch University, where he is currently a Distinguished Professor of electrical machines and drives. His research interests include computer-aided design and the control of reluctance, permanent magnet, and induction electrical machine drives, with applications in electric transportation and renewable energy. He is a South African National Research Foundation-rated Scientist and a registered Professional Engineer in South Africa.



RONG-JIE WANG (Senior Member, IEEE) received the M.Sc. (Eng.) degree in electrical engineering from the University of Cape Town, South Africa, in 1998, and the Ph.D. degree in electrical engineering from Stellenbosch University, South Africa, in 2003. He is currently a Professor with the Department of Electrical and Electronic Engineering, Stellenbosch University. His research interests include novel topologies of permanent magnet machines, computer-aided design and optimisation of electrical machines, cooling design and analysis, and renewable energy systems. He is a South African National Research Foundation-rated Researcher and a registered Professional Engineer in South Africa.



ABDOULKADRI CHAMA received the M.Sc. degree in applied mathematics from the University of KwaZulu-Natal, South Africa, and the Ph.D. degree in applied mathematics from the University of Cape Town, South Africa, in 2014. He has held several postdoctoral research positions in both the United States and South Africa. His research interest includes computational mathematics, with a speciality in finite element methods.

...